

A probabilistic description of entrainment instability for cloud-topped boundary-layer models

Jun Yin,^a John D. Albertson^b and Amilcare Porporato^{a*}

^aDepartment of Civil and Environmental Engineering, Pratt School of Engineering, Duke University, Durham, NC, USA

^bSchool of Civil and Environmental Engineering, Cornell University, Ithaca, NY, USA

*Correspondence to: A. Porporato, Civil and Environmental Engineering Department, Duke University, Durham, NC, USA.
E-mail: amilcare.porporato@duke.edu

Cloud-top radiative and evaporative cooling effects on entrainment fluxes are essential to turbulence generation and growth of cloud-topped boundary layers. While the cloud radiative cooling effects are currently not well understood, their interaction with the cloud-top evaporation further complicates efforts to parametrize the phenomena due to the random behaviour of the turbulent mixing at the cloud-top interface. Here we focus on the cloud-top mixing and treat the typical turbulent mixing eddy in a statistical manner to relate the mean evaporative cooling rate to the distribution of effective mixing fraction (defined as the fraction of air coming from the free atmosphere that enhances the entrainment flux). Existing observations suggest that this effective mixing fraction can be parsimoniously parametrized with beta distributions, the shape parameters of which control the locations of stability lines in the Cloud-Top Entrainment Instability (CTEI) diagrams used to discriminate between stable and unstable clouds. The probabilistic description of the cloud-top mixing process allows us to coherently reinterpret various forms of CTEI criteria and generalize them to form new cloud-top entrainment schemes. We expect that such schemes will help improve cloud dynamic models by embedding realistic distributions of the effective mixing fraction.

Key Words: cloud-top entrainment instability; cloud-topped boundary layer; entrainment parametrization; convection; evaporative cooling; mixing fraction; mixed layer; slab model

Received 24 February 2016; Revised 8 October 2016; Accepted 17 October 2016; Published online in Wiley Online Library 21 December 2016

1. Introduction

The phase change of atmospheric water vapour during low-level cloud formation alters the distribution of short-wave and long-wave radiation and modulates the cloud-top entrainment flux and boundary-layer dynamics (Garratt, 1992; Houze, 1993; Boucher *et al.*, 2013; Zhang *et al.*, 2013). While several cloud parametrization schemes have been proposed since the pioneering work of Lilly (1968), the complexity of the underlying processes remains a vexing difficulty for atmospheric models. Indeed, cloud feedbacks are arguably one of the largest sources of uncertainty in climate predictions (Bony and Dufresne, 2005; Stephens, 2005; Bony *et al.*, 2006; Stevens, 2006; Boucher *et al.*, 2013). Improved cloud parametrization schemes are also essential to hydroclimatic models, which are often used to analyze land–atmosphere interaction and atmospheric transport processes (Ek and Holtslag, 2004; Juang *et al.*, 2007; Betts, 2009; Gentine *et al.*, 2013a; Yin *et al.*, 2015).

Parametrizations of low-level stratocumulus clouds should specifically account for radiative and evaporative cooling effects, which are among the most important driving forces for the dynamics of the cloud-topped boundary layer (CTBL; Garratt, 1992; Lock, 1998; Moeng *et al.*, 1999; Stevens, 2005; de Lozar and Mellado, 2015a). These two cooling mechanisms have significant

impacts on the buoyancy of the parcels at the top of the cloud and generate turbulence within the boundary layer (Deardorff, 1976; Stull, 1988; Shao *et al.*, 1997; Lock and Macvean, 1999a; de Lozar and Mellado, 2015a). While the radiative cooling rate can be quantified relatively well by analyzing radiation components and cloud properties (Yamamoto *et al.*, 1970; Stephens, 1978a, 1978b), tracking the evaporative cooling rate is less straightforward, especially because of the random nature of the turbulence and mixing at the cloud-top interface (Sullivan *et al.*, 1998; Mellado *et al.*, 2010b; Yamaguchi and Feingold, 2013). In addition, these cooling rates are influenced by the cloud microphysical parameters, such as cloud droplet size, which are critical to the cloud formation and atmospheric radiation profiles (Árnason and Greenfield, 1972; Stephens, 1978a; Martin *et al.*, 1994; Wood, 2012). Previous studies on evaporative cooling effects have focused more on the buoyancy change of mixed air and less on the cooling rate itself. For example, under certain conditions, the mixed air can be denser than the surrounding cloud, thus leading to unstable cloud layers, a process termed cloud-top entrainment instability (CTEI; Lilly, 1968; Randall, 1980; Deardorff, 1980b). This buoyancy change due to cloud-top evaporation has been incorporated into entrainment closures to simulate dynamics of CTBL (Nicholls and Turton, 1986; Lock, 1998; Lock and Macvean, 1999b; Lilly, 2002a, 2002b). Some

diagnostic methods have been used to estimate the evaporative cooling rate from observations, such as by using ozone as a tracer (Nicholls and Turton, 1986; Wang and Albrecht, 1994; Shao *et al.*, 1997). However, a complete quantification of the evaporative cooling rate along with a coherent coupling with the CTBL prognostic equations is still lacking.

In this study, we focus on the evaporative cooling effects on turbulence generation in a CTBL model. To quantify this cooling rate, we analyze the cloud-top mixing process through considering a ‘typical’ turbulent eddy with emphasis on the effective mixing fraction, defined as the fraction of air coming from the free atmosphere that enhances the entrainment flux as discussed in de Lozar and Mellado (2015a). Based on both flight observations (Albrecht *et al.*, 1988; Wang and Albrecht, 1994; Shao *et al.*, 1997) and direct numerical simulations (Mellado *et al.*, 2010b), there is evidence to support treating the effective mixing fraction as a random variable following a beta distribution. The resulting cloud-top mixing scheme allows us to consistently re-interpret various CTEI criteria in relation to their implicit parametrization of the probabilistic properties of the cloud-top mixing.

The article is organized as follows: section 2 extends the cloud-free entrainment scheme to include cloud-top radiative and evaporative cooling effects. Section 3 quantifies the mean evaporative cooling rate by statistically treating a typical turbulent mixing eddy. Section 4 links this mean cooling rate to various CTEI criteria and the distribution of mixing fraction, which is further analyzed in section 5 and fitted as a beta distribution. Section 6 performs a sensitivity analysis of the shape parameters on CTEI diagrams. Section 7 applies the CTBL model to a nocturnal stratocumulus case and compares the simulation results with observations. Final conclusions are summarized in section 8. The CTBL and CTEI equations are reviewed in the Appendices along with several less essential components of the models.

2. Entrainment

The most essential part in a CTBL model is the entrainment parametrization, which involves connecting the entrainment flux to both the buoyancy inversion strength and other known boundary-layer variables (Appendix A briefly reviews the relevant conservation equations and defines the notation). To connect to the buoyancy inversion strength, we use virtual potential temperature (θ_v) as the conventional surrogate for density in buoyancy calculations (Emanuel, 1994),

$$\theta_v = \theta \left[1 + \left(\frac{R_v}{R_d} - 1 \right) q - q_L \right], \quad (1)$$

where θ is potential temperature, q is specific humidity, q_L is liquid water content, R_v and R_d are the gas constant for water vapour and dry air, respectively. The governing equation for the virtual potential temperature in the horizontally homogenous turbulent flow can be expressed as (Stull, 1988),

$$\frac{\partial \theta_v}{\partial t} + w_l \frac{\partial \theta_v}{\partial z} = - \frac{1}{\rho c_p} \frac{\partial \bar{F}}{\partial z} - \frac{\partial \overline{w'\theta_v'}}{\partial z}, \quad (2)$$

where w_l is large-scale vertical velocity, ρ is air density, c_p is specific heat of air at constant pressure, \bar{F} is horizontally average source rate (e.g. evaporative and radiative terms), and $\overline{w'\theta_v'}$ is the vertical buoyancy flux. The overbars and primes denote the mean and turbulent parts of the variables. For simplicity of notation and following conventional practice (e.g. Lilly, 1968; Tennekes, 1973), the overbars for the temperature and humidity in the mixed-layer equations are not indicated. Applying Leibnitz’s rule and integrating (2) with respect to z between the boundary-layer top ($z = h-$) and the free atmosphere just above the boundary layer ($z = h+$) yields,

$$-(\overline{\theta_v'w'})_{h-} = \Delta\theta_v \left(\frac{dh}{dt} - w_l \right) - \frac{\Delta\bar{F}}{\rho c_p}, \quad (3)$$

where $(\overline{\theta_v'w'})_{h-}$ is the entrainment flux at $h-$, the operator Δ denotes the change of the corresponding mean variable across the inversion, and $\Delta\bar{F}$ is the net cooling source inside the inversion layer from $h-$ to $h+$. Clearly, $\Delta\bar{F}$ depends on the location of the inversion and the vertical profiles of cooling/heating sources such as cloud-top evaporation and cloud-top long-wave/short-wave radiations (Lock, 1998; Moeng *et al.*, 1999; de Lozar and Mellado, 2015b). $\Delta\bar{F}$ also depends on cloud microphysical parameters such as cloud condensation nuclei, which are necessary for the cloud formation and further influence the timing and rates of evaporation (Houze, 1993; Martin *et al.*, 1994; Wood, 2012). Unlike the in-cloud cooling indirectly influencing the entrainment rate as explained later in (5), the cooling inside the inversion layer ($\Delta\bar{F}$), termed direct cooling (Moeng *et al.*, 1999; Stevens, 2002), appears explicitly in the entrainment rate equation. While there is no consensus on the importance of these direct cooling effects (Turton and Nicholls, 1987; Lock and Macvean, 1999a; Wood, 2012), here we follow the procedure of Deardorff (1976) and assume that only a fraction of the total cooling/heating sources is inside the inversion layer and directly influences the entrainment rate. As a result,

$$\frac{\Delta\bar{F}}{\rho c_p} = \alpha_E \frac{\lambda \bar{E}_c}{\rho c_p} + \alpha_R \frac{\bar{R}_c}{\rho c_p}, \quad (4)$$

where $\lambda \bar{E}_c$ is total cloud-top evaporative cooling rate, \bar{R}_c is the net cloud-top radiative cooling rate, and α_E and α_R are the fraction coefficients. More detailed partitioning method for direct and indirect cooling, based on the definition of inversion points and radiation profiles as described in de Lozar and Mellado (2015b), will be investigated in further contributions.

The second step of parametrizing the entrainment flux has always been a challenge for the CTBL (Moeng *et al.*, 1999; Stevens, 2002; de Lozar and Mellado, 2015b). The presence of clouds allows the radiative divergence at the cloud top to influence the vertical distribution of buoyancy flux and generate additional turbulence kinetic energy to accelerate the entrainment process (Stull, 1988; Moeng *et al.*, 1999; Lilly, 2002a). Besides the radiative cooling, the mixing of entrained dry air causes some evaporation in the clouds below and this evaporation process under certain conditions makes the mixed air denser than the surrounding clouds, thus reversing the buoyancy and potentially accelerating the entrainment process (Randall, 1980; Deardorff, 1980b; Nicholls and Turton, 1986; Stevens, 2002). Here, we start from a simple strategy proposed by Lock and Macvean (1999a), which assumes the entrainment flux is proportional to the sum of surface heat flux and cloud-top radiative cooling. Lilly (2002a) argued that different weights should be assigned for each type of heating or cooling sources when parametrizing the entrainment flux. We therefore extend these schemes and model the most important turbulence generation sources in the CTBL with different weighting coefficients. As a result,

$$-(\overline{w'\theta_v'})_{h-} = A_0 \frac{\theta_0 u_*^3}{gh} + A_1 (\overline{w'\theta_v'})_0 + A_2 \frac{\lambda \bar{E}_c}{\rho c_p} + A_3 \frac{\bar{R}_c}{\rho c_p}, \quad (5)$$

where subscripts $h-$ and 0 refer to the flux locations at the top of the boundary layer and near the Earth surface, respectively, A_0 , A_1 , A_2 , and A_3 are the coefficients weighting the importance of each term, u_* is friction velocity, g is gravitational acceleration, λ is latent heat of vaporization, $\lambda \bar{E}_c$ is mean evaporative cooling rate, and \bar{R}_c is the cloud-top radiative cooling rate (Appendix B). The first two terms on the right-hand side of (5) account for the entrainment fluxes due to shear-driven and buoyancy-generated turbulence as in cloud-free boundary-layer models (Tennekes, 1973; Stull, 1976; Garratt, 1992; Porporato, 2009; Rigby *et al.*, 2015). The last two terms account for evaporative cooling effects by directly linking the cooling rates ($\lambda \bar{E}_c$ and \bar{R}_c) to the cloud-top

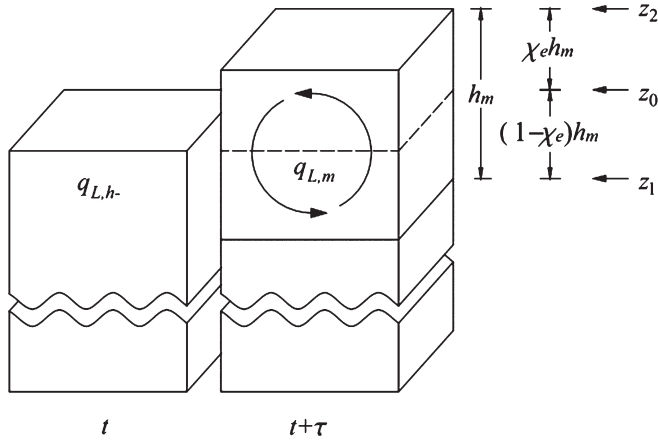


Figure 1. Schematic representation of the entrainment mixing in the cloud-topped boundary layer from time t to $t + \tau$.

buoyancy flux. Substituting (5) into (3) yields,

$$\Delta\theta_v \left(\frac{dh}{dt} - w_l \right) = B_0 \frac{\theta_0 u_*^3}{gh} + B_1 (\overline{w'\theta_v'})_0 + B_2 \frac{\lambda \overline{E_c}}{\rho c_p} + B_3 \frac{\overline{R_c}}{\rho c_p} \quad (6)$$

where $B_0 = A_0$, $B_1 = A_1$, $B_2 = A_2 + \alpha_E$, $B_3 = A_3 + \alpha_R$. The coefficient B_0 is typically around 2.5 and B_1 may range from 0.1 to unity with a typical value of 0.2 (Tennekes, 1973; Stull, 1976; Porporato, 2009). The coefficient B_3 is on the order 0.4–0.5 according to smoke-cloud boundary-layer studies (Lilly, 2002a). As discussed later, this general parametrization scheme is consistent with prior studies of CTBL and CTEI (section 4).

3. Evaporative cooling rate

Mixing of dry air from the free atmosphere into the cloud top causes some of the liquid water to evaporate, thereby cooling the surrounding air. This process can be analyzed by focusing on the cloud-top entrainment process over a typical mixing time-scale, τ . This scale is assumed to be large enough to average over several turbulent eddy turnovers but short enough compared to the time-scale of the growth of the ABL. The mixing is considered to take place in the cloud-top interface over a typical vertical eddy size, h_m , as illustrated in Figure 1. The typical eddy vertically crosses the cloud-top interface and thus corresponds to the depth of entrainment zone of the CTBL. The fraction of air coming from the free atmosphere, defined as mixing fraction, χ , is highly variable in space and time and therefore should be treated as a random variable. The statistical properties of χ at different levels and times for stratocumulus-topped mixed layers have been investigated by Mellado *et al.* (2010b) using direct numerical simulations.

Because of the role of free atmosphere air in this process, it is only the mixing near the cloud-top interface that tends to impact cloud instability (de Lozar and Mellado, 2015a). We can thus refer to an ‘effective mixing process’, characterized by an effective mixing fraction, $0 \leq \chi_e \leq 1$, with probability density function (pdf) $f(\chi_e)$. $\chi_e = 0$ means that no air coming from the free atmosphere is involved in the mixing, while $\chi_e = 1$ corresponds to the case of pure mixing of air from the free atmosphere. Accordingly, for a ‘typical’ mixing eddy of vertical size h_m , $\chi_e h_m$ is the depth of air coming from free atmosphere and $(1 - \chi_e) h_m$ is the depth of air coming from the boundary layer.

Evaporative cooling by vaporization of cloud liquid water can be described as

$$\lambda E_c = \lambda \frac{W(t) - W(t + \tau)}{\tau}, \quad (7)$$

where W is the liquid water path between z_1 and z_2 within the eddy in question:

$$W(t) = \int_{z_1}^{z_2} \rho q_L(z, t) dz. \quad (8)$$

In the previous expression $q_L(z, t)$ is the liquid water content at time t at level z inside the eddy, approximated in a binary fashion as

$$q_L(z, t) = \begin{cases} q_{L,h-} & z_1 < z < z_0 \\ 0 & z_0 < z < z_2, \end{cases} \quad (9)$$

where the subscript $h-$ refers to the value just below the inversion (z_0). This assumes negligible fluctuations in liquid water content near the top of the cloud within the time-scale τ and also negligible liquid water in the free atmosphere above the cloud.

After a time τ , one has well-mixed conditions and the liquid water content is

$$q_L(z, t + \tau) = q_{L,m}, \quad (10)$$

where the subscript m refers to mixed air. Substitution of (8), (9), and (10) into (7) yields the evaporative cooling rate,

$$\lambda E_c = \frac{\lambda \rho h_m}{\tau} [(1 - \chi_e) q_{L,h-} - q_{L,m}], \quad (11)$$

which is related to the liquid water content of the mixed air. The ratio h_m/τ , which describes the mixing intensity, may be assumed to be proportional to the entrainment velocity,

$$\frac{h_m}{\tau} = k \left(\frac{dh}{dt} - w_l \right), \quad (12)$$

where k is a proportionality coefficient. A similar heuristic parametrization was employed by Gentine *et al.* (2013b) for modelling the growth rate of the mixed layer using an eddy overturning time-scale; here it is adopted heuristically, supported by the interesting connections that it provides especially in relation to the CTEI (section 4) as well as by the good results provided when modelling the evolution of CTBL (section 7), leaving to further research its more rigorous justification. Substituting (12) into (11),

$$\lambda E_c = \lambda \rho k \left(\frac{dh}{dt} - w_l \right) [(1 - \chi_e) q_{L,h-} - q_{L,m}], \quad (13)$$

where $q_{L,m}$ is a nonlinear function of effective mixing fraction (Appendix C). Equation (13) provides an interesting link between evaporative cooling and boundary-layer dynamics. However, the liquid water content q_L is not a convenient variable for the study of the cloud instability, since CTEI criteria are typically expressed using virtual potential temperature (e.g. Kuo and Schubert, 1988). To make the needed connection we start from liquid water potential temperature θ_L , which is a conserved variable (Deardorff, 1980a, also Appendix A) and can be expressed with sufficient accuracy as (Betts, 1973; Garratt, 1992)

$$\theta_L = \theta - \frac{\lambda}{c_p} q_L. \quad (14)$$

This definition (14) is then applied to the air at the top of the boundary layer,

$$\theta_{L,h-} = \theta_{h-} - \frac{\lambda}{c_p} q_{L,h-}, \quad (15)$$

and to the mixed air,

$$\theta_{L,m} = \theta_m - \frac{\lambda}{c_p} q_{L,m}. \quad (16)$$

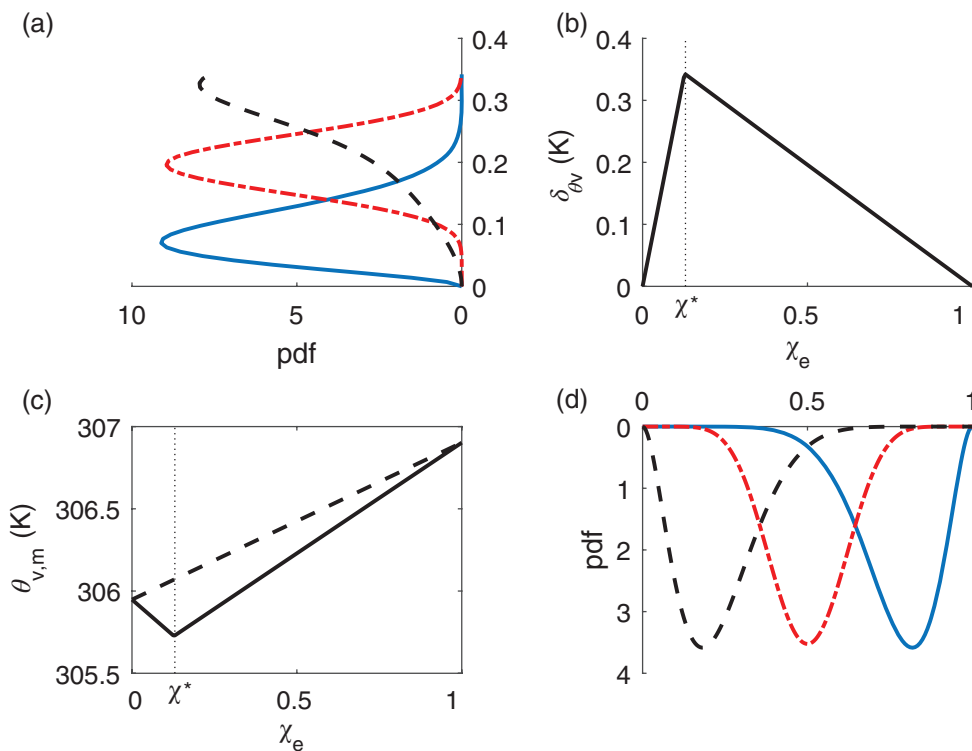


Figure 2. (a) PDF of evaporative cooling temperature (δ_{θ_v}) derived from (b) the relationship between δ_{θ_v} and χ_e or (c) between $\theta_{v,m}$ and χ_e , where χ_e is assumed to follow (d) beta distributions $\beta(10, 3)$ (solid lines), $\beta(10, 10)$ (dash-dot lines), $\beta(3, 10)$ (dashed lines). [Colour figure can be viewed at wileyonlinelibrary.com].

This liquid water potential temperature is conserved during the moist adiabatic mixing, so that (Betts and Albrecht, 1987)

$$\theta_{L,m} = (1 - \chi_e)\theta_{L,h-} + \chi_e\theta_{L,h+}. \quad (17)$$

Combining (15), (16) and (17), and substituting into (13) yields

$$\lambda E_c = \rho c_p k \left(\frac{dh}{dt} - w_l \right) [(1 - \chi_e)\theta_{h-} + \chi_e\theta_{h+} - \theta_m]. \quad (18)$$

To connect this cooling rate to the virtual potential temperature of the mixed air, we rewrite the evaporative cooling rate in (18) as

$$\lambda E_c = \rho c_p k \zeta \left(\frac{dh}{dt} - w_l \right) \delta_{\theta_v}, \quad (19)$$

where

$$\delta_{\theta_v} = (1 - \chi_e)\theta_{v,h-} + \chi_e\theta_{v,h+} - \theta_{v,m}. \quad (20)$$

and

$$\zeta = \frac{(1 - \chi_e)\theta_{h-} + \chi_e\theta_{h+} - \theta_m}{(1 - \chi_e)\theta_{v,h-} + \chi_e\theta_{v,h+} - \theta_{v,m}}. \quad (21)$$

Note that the ratio ζ establishes a relationship between potential temperature and virtual potential temperature of air before and after mixing. This ratio tends to be constant around 1.2–1.3 for typical stratocumulus clouds, as shown in Appendix D. $\theta_{v,m}$ is a nonlinear function of effective mixing fraction (Appendix C) and can be approximated as a piecewise linear function (Shao *et al.*, 1997; Yamaguchi and Randall, 2008) (solid lines in Figure 2(c)). The virtual potential temperature drop δ_{θ_v} during the evaporative cooling process can be interpreted as the difference between mixing temperature without evaporation (the first two terms in (20) shown as the dashed line in Figure 2(c)) and the real mixing temperature (the last term in (20) shown as the solid line in Figure 2(c)). The relationship between δ_{θ_v} and χ_e (Figure 2(b)) allows us to derive the distribution of evaporative cooling temperature as illustrated in Figure 2(a),

once the distributions of mixing fraction (Figure 2(d), e.g. beta distribution as will be discussed in section 5) are found.

The horizontal average value of evaporative cooling rate in (19) can be estimated as,

$$\lambda \bar{E}_c = \rho c_p k \zeta \left(\frac{dh}{dt} - w_l \right) \int_0^1 [(1 - \chi_e)\theta_{v-} + \chi_e\theta_{v+} - \theta_{v,m}(\chi_e)] f(\chi_e) d\chi_e. \quad (22)$$

With this expression we are now ready to study the buoyancy effect of evaporative cooling in terms of virtual potential temperature.

4. Linking cloud-topped boundary layer to cloud-top entrainment instability (CTEI)

The mean evaporative cooling rate derived above can now be combined with the entrainment parametrization scheme to interpret prior studies of CTEI. To do so, we first substitute (22) into (6), so that

$$\left(\frac{dh}{dt} - w_l \right) \Delta \tilde{\theta}_v = B_0 \frac{\theta_0 u_*^3}{gh} + B_1 (\overline{w'\theta_v'})_0 + B_3 \frac{\bar{R}_c}{\rho c_p}, \quad (23)$$

where

$$\Delta \tilde{\theta}_v = \Delta \theta_v - B_2 k \zeta \int_0^1 [(1 - \chi_e)\theta_{v,h-} + \chi_e\theta_{v,h+} - \theta_{v,m}(\chi_e)] f(\chi_e) d\chi_e. \quad (24)$$

Here, $\Delta \theta_v$ is the buoyancy inversion strength and the remaining term represents the evaporating cooling rate without boundary-layer growth rate (dh/dt). Therefore, $\Delta \tilde{\theta}_v$ gives the buoyancy inversion strength as it is impacted by evaporative cooling effects. Under unsaturated conditions, θ_v is a conserved variable during the cloud-top mixing process so that $\theta_{v,m} = (1 - \chi_e)\theta_{v,h-} + \chi_e\theta_{v,h+}$ and therefore $\Delta \tilde{\theta}_v = \Delta \theta_v$ for any k and B_2 and any distribution of χ_e . This directly transforms (23) into the entrainment parametrization schemes

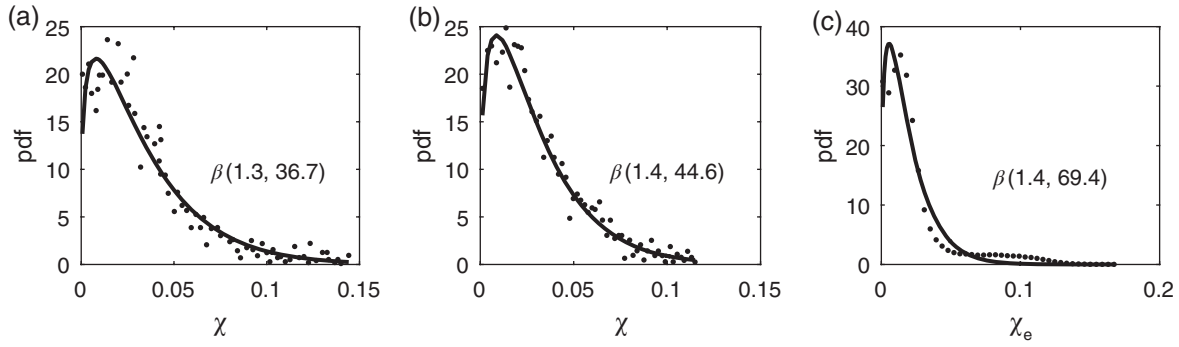


Figure 3. Distributions of mixing fractions and corresponding fit with beta pdfs: (a) flight observations at one horizontal level by Wang and Albrecht (1994), (b) flight observations at one horizontal level by Shao *et al.* (1997), (c) direct numerical simulation of averaged mixing fraction at three horizontal levels (Mellado *et al.*, 2010b).

for the cloud-free or smoke-cloud boundary-layer model. When $\Delta\tilde{\theta}_v$ approaches zero, one may expect from (23) that, in order to keep the right-hand side finite, the growth rate of the boundary layer becomes very large. This suggests that the cloud top tends to become unstable, consistent with the physical interpretation of CTEI (Deardorff, 1980b; Randall, 1984; Lilly, 2002b).

The connection between $\Delta\tilde{\theta}_v$ in (24) and cloud-top instability can be further analyzed as follows. As reviewed in Appendix E, the CTEI is given in terms of the buoyancy difference between the mixed air and the surrounding cloud air, $\theta_{v,m}(\chi_e) - \theta_{v,h-}$, which also appears inside the integral term of (24). This common term allows us to connect $\Delta\tilde{\theta}_v$ to various CTEI criteria:

- i) Assuming $B_2 = 1/(\zeta k \chi^*)$ and a sharp distribution of effective mixing fraction $f(\chi_e) = \delta(\chi_e - \chi^*)$ in which χ^* is the saturation mixing fraction (see Appendix D) and $\delta(\bullet)$ is Dirac delta function such that the effective mixing fraction at saturation determines the cloud stability, $\Delta\tilde{\theta}_v$ in (24) becomes

$$\Delta\tilde{\theta}_v = \frac{\theta_{v,m}(\chi^*) - \theta_{v,h-}}{\chi^*}, \quad (25)$$

which is the CTEI defined by Randall (1980) and Deardorff (1980b) as listed in (E1).

- ii) Assuming χ is uniformly distributed as in Nicholls and Turton (1986) and $B_2 = 2/(\zeta k)$, $\Delta\tilde{\theta}_v$ in (24) becomes,

$$\Delta\tilde{\theta}_v = 2 \int_0^1 [\theta_{v,m}(\chi) - \theta_{v,h-}] d\chi, \quad (26)$$

which is the Δ_{NT} defined by Nicholls and Turton (1986) as listed in (E2) for parametrizing the entrainment rate (Turton and Nicholls, 1987; Stevens, 2002). Note that Δ_{NT} appears in the numerator of the entrainment equation in Nicholls and Turton (1986) and cannot be used to predict the cloud-top instability condition.

- iii) Assuming, instead, that $1/\chi$ is uniformly distributed as in Duynkerke (1993) and $B_2 = 1/(\zeta k)$, $\Delta\tilde{\theta}_v$ in (24) becomes,

$$\Delta\tilde{\theta}_v = \int_0^1 \frac{\theta_{v,m}(\chi) - \theta_{v,h-}}{\chi} d\chi. \quad (27)$$

which is the CTEI defined by Duynkerke (1993) as listed in (E3).

The correspondence between $\Delta\tilde{\theta}_v$ in (24) and existing CTEI criteria is useful to compare and extend them as well as to combine them consistently with entrainment parametrization schemes in CTBL models. For example, the CTEI criterion defined by Randall (1980) and Deardorff (1980b) as listed in (E1) is the denominator of the entrainment rate expression in the CTBL model of Stage and Businger (1981), which was derived from the turbulence kinetic energy balance (Randall, 1984; Rogers

et al., 1985). Moreover, one can also find new entrainment parametrization schemes by replacing $\Delta\tilde{\theta}_v$ in (23) with various CTEI criteria such as those listed in (E2) and (E3). More generally, the new cloud parametrization schemes from (23) and (24) are expected to be more accurate with more realistic distributions of effective mixing fraction (e.g. beta distribution), as discussed next.

5. Distribution of mixing fraction

As discussed in section 3, the cloud-top mixing at different levels contribute differently to the entrainment process (de Lozar and Mellado, 2015a). Thus the distribution of effective mixing fraction therefore may be expressed as a weighted average,

$$f(\chi_e) = \int_0^\infty p(\chi, z) \omega(z) dz, \quad (28)$$

where $p(\chi, z)$ is the pdf of χ at altitude z and the weighting function $\omega(z)$ (satisfying $\int_0^\infty \omega(z) dz = 1$) is constructed so as to give larger weight at the cloud-top interface.

The statistics of stratocumulus clouds have been extensively characterized by Albrecht *et al.* (1988) and Wang and Albrecht (1994), where the latter used ozone as a tracer to obtain the empirical pdf of mixing fraction at horizontal flight leg 3 (about 770 m) (dots in Figure 3(a)). In this figure, a beta distribution (solid line) is shown to fit the observations well. A similar diagnostic method was applied by Shao *et al.* (1997), and the resulting pdf of mixing fraction is shown as dots in Figure 3(b); this too is well approximated by a beta distribution. We note that flight height variation may influence the accuracy of mixing fraction estimation and for this reason the data at three different levels of Mellado *et al.* (2010b) obtained from direct numerical simulations were used to further analyze the statistics of mixing fraction. When combined with equal weights (due to the fact that these three levels are close to the entrainment zone) to represent the effective mixing process, the mixing fraction can also be described by a beta distribution (Figure 2(c)). In general, a beta distribution for the random variable χ ($0 \leq \chi \leq 1$) with two positive shape parameters β_1 and β_2 is defined as (Davison, 2003),

$$f(\chi) = \frac{\Gamma(\beta_1 + \beta_2)}{\Gamma(\beta_1)\Gamma(\beta_2)} \chi^{\beta_1-1} (1-\chi)^{\beta_2-1}, \quad (29)$$

where $\Gamma(\bullet)$ is the gamma function. The mean of the distribution is

$$\mu_\chi = \frac{\beta_1}{\beta_1 + \beta_2}, \quad (30)$$

and the standard deviation is

$$\sigma_\chi = \sqrt{\frac{\beta_1 \beta_2}{(\beta_1 + \beta_2)^2 (\beta_1 + \beta_2 + 1)}}. \quad (31)$$

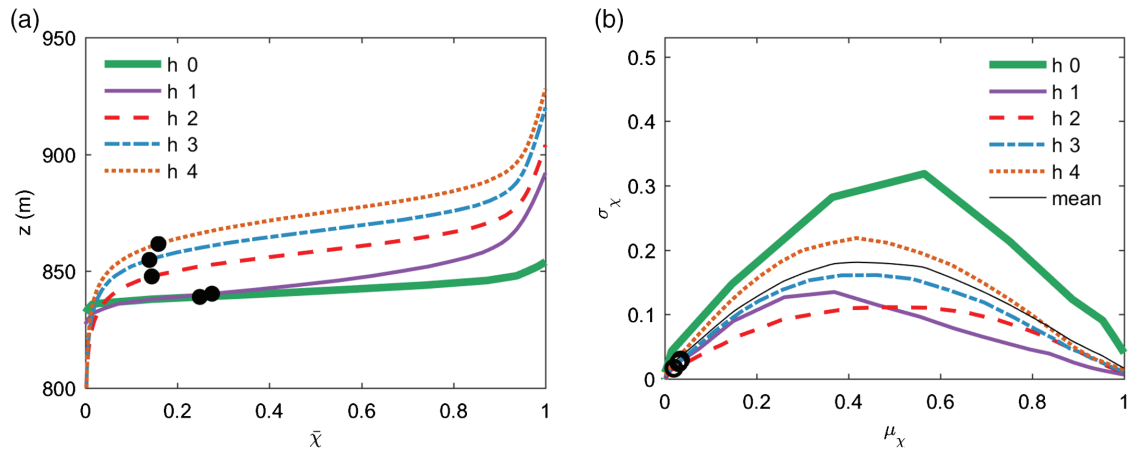


Figure 4. (a) Profiles of mean mixing fraction and (b) relationships between mean and standard deviation of mixing fraction at different times from profile statistics of LES for the case RF01 of the DYCOMS-II (Stevens *et al.*, 2005). The dots in (a) indicate the values of mean mixing fraction at the inversion levels. The circles in (b) indicate the relationship between mean and standard deviation of mixing fraction from the fitted distributions in Figure 3. [Colour figure can be viewed at wileyonlinelibrary.com].

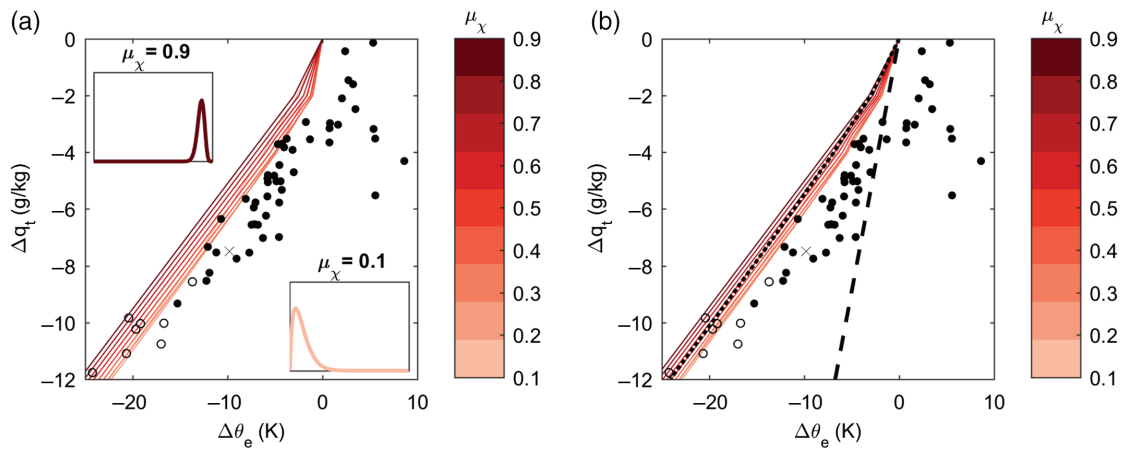


Figure 5. CTEI diagrams in the $(\Delta\theta_e, \Delta q_t)$ plane with beta-distributed mixing fraction, where its mean and standard deviation relationship follows the dash-dot lines in Figure 4. The boundary-layer variables refer to (a) the RF01 case of DYCOMS-II (Stevens *et al.*, 2005) and (b) case K from Yamaguchi and Randall (2008). The insets show the pdf of effective mixing fractions of the beta distribution with extreme parameter values. The dots are observational data collected by Kuo and Schubert (1988) with open dots for trade cumulus cases and solid dots for stratocumulus. The x-marks refer to the RF01 case of DYCOMS-II (Stevens *et al.*, 2005). The dashed and dotted lines in (b) represent the Randall–Deardorff and Duynkerke CTEI criteria, respectively. [Colour figure can be viewed at wileyonlinelibrary.com].

As discussed above, this beta distribution with only two parameters appears both accurate and flexible enough to model the distribution of mixing fraction for the cloud-top entrainment process.

To further analyze the shape parameters β_1 and β_2 , we explored the intercomparison study between the large-eddy simulations (LESs) and the first research flight (RF01) of the second Dynamics and Chemistry of Marine Stratocumulus (DYCOMS-II; Stevens *et al.*, 2005). To do so, the mixing fraction is approximated from the normalized liquid water potential temperature,

$$\chi(z) \approx \frac{\theta_L(z) - \langle\theta_L\rangle}{\theta_{L,h+} - \langle\theta_L\rangle}, \quad (32)$$

where $\langle\theta_L\rangle$ is the average liquid water potential temperature in the boundary layer, and $\theta_{L,h+}$ is the liquid water potential temperature just above the boundary layer in the free atmosphere, where the liquid water content approaches zero. Although this approximation should be used with caution (Albrecht *et al.*, 1985; Mellado *et al.*, 2010a), it is helpful to analyze some general statistics of the mixing fraction from LES (Stevens *et al.*, 2005). The statistics of multiple LES results (http://gcss-dime.giss.nasa.gov/dycoms-ii/modsim_dycoms-ii_gcss7-rf01.html; accessed 6 November 2016) were used in (32) to find the profile of the mixing fraction and the $\mu_\chi \sim \sigma_\chi$ relationship. As can be seen in Figure 4(a), the mean mixing fraction profiles show curves of sigmoid shape, which are consistent with direct numerical simulation results in previous research (Mellado, 2010; Mellado *et al.*, 2010b). Relatively low mean mixing fraction is observed at

the inversion level, defined as the $q_t = 8 \text{ g kg}^{-1}$ contour (Stevens *et al.*, 2005), where the mixing of clear and cloudy air is expected to be strong. This low value is corresponding to the low saturation mixing fraction of 0.09 in the RF01 of the DYCOMS (Mellado *et al.*, 2010b). Further study of the potential connections between saturation mixing fraction and mixing fraction at the inversion level under more general conditions will be the subject of future research. Figure 4(b) also shows the typical relationship between mean and standard deviation of mixing fraction during the 4 h simulation period. Such a relationship may be used to reduce the number of parameters used in entrainment modelling.

6. Control of shape parameters on CTEI diagrams

The shape parameters determine the distribution of mixing fraction and consequently control the cloud instability. To explore the importance of these shape parameters, we consider the $(\Delta\theta_e, \Delta q_t)$ plane (Figure 5), which is extensively used in CTEI studies (Kuo and Schubert, 1988; MacVean and Mason, 1990; Duynkerke, 1993; Yamaguchi and Randall, 2008) to define the stability conditions of the cloud-top interface. In particular, marginal stability lines divide the plane into two parts, the right part corresponding to stable clouds and the left part to unstable clouds. The data points, taken from Kuo and Schubert (1988), show both persistent stratocumulus (solid dots) and less stable trade cumulus (open dots). For this reason, the relative stability of the clouds can be estimated by a new dimensionless parameter $k = \Delta\theta_e / (\lambda / c_p \Delta q_t)$, which has larger value for less stable clouds (Kuo and Schubert,

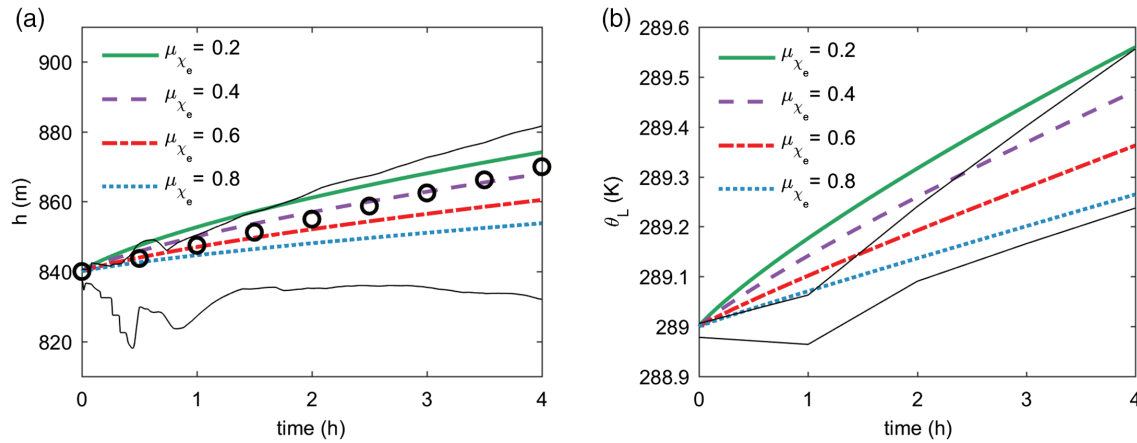


Figure 6. Dynamics of (a) boundary-layer height, and (b) liquid water potential temperature with different distributions of mixing fraction. The thin lines are the maximum and minimum values within the master ensemble of LES for the case RF01 of the DYCOMS-II (Stevens *et al.*, 2005), and the circles show the observed evolutions of cloud top with boundary-layer growth rate 7.5 m h^{-1} (Stevens *et al.*, 2003). [Colour figure can be viewed at wileyonlinelibrary.com].

1988; Yamaguchi and Randall, 2008). Figure 5(a) presents various stability lines where the novel CTEI criterion $\Delta\theta_v$ equals zero with boundary-layer variables referring to the case RF01 of the DYCOMS-II. For simplicity, we approximate the weighting function for χ_e as a Dirac delta function $\omega(z) = \delta(z - z_i)$, in which z_i is the location where there is the most intensive mixing of clear and cloudy air. For mixing fraction, σ_χ is modelled as an empirical function of μ_χ as in the dash-dot curve in Figure 4(b). To separate the most unstable trade cumulus from the stable stratocumulus for the marginal stability line, the multiplicative coefficient B_2k is set to 4 and μ_χ is around 0.2 (curves in lighter color in Figure 5(a)), which is close to the mean value of the mixing fraction at the inversion height. According to this diagram, the RF01 of DYCOMS-II is identified as the stable condition, which is consistent with the observations (Stevens *et al.*, 2003). Note that both the liquid water content and temperature at the top of the cloud may have certain impacts on the pattern of the $(\Delta\theta_e, \Delta q_t)$ plane (Duykerke, 1993; Yamaguchi and Randall, 2008; Yue *et al.*, 2013). Figure 5(b) shows the similar diagram with boundary-layer variables defined as the case K from Yamaguchi and Randall (2008), which is 8 K warmer but has similar amount of liquid water content as the RF01 of the DYCOMS-II. For comparison, two other marginal stability lines from the Randall–Deardorff and Duykerke CTEI criteria are also plotted in Figure 5(b). While the Randall–Deardorff criterion clearly overestimates the effects of cloud-top mixing on its instability, the Duykerke criterion is more consistent with our result.

7. Boundary-layer dynamics with CTEI parametrization

To explore the sensitivity of boundary-layer dynamics to the distributions of mixing fractions, we now model the CTBL corresponding to the RF01 case of DYCOMS-II, characterized by unbroken marine nocturnal stratocumulus clouds that have been extensively studied using LESs and direct numerical simulations (Stevens *et al.*, 2005; Mellado, 2010; Mellado *et al.*, 2010a; de Lozar and Mellado, 2015b). The initial sounding profiles were set as in equations (1) and (2) in Stevens *et al.* (2005), with $\theta_L = 289 \text{ K}$ and $q_t = 9 \text{ g kg}^{-1}$ at the top of the clouds ($h = 840 \text{ m}$) and $\theta_L = 297.5 \text{ K}$ and $q_t = 1.5 \text{ g kg}^{-1}$ just above the clouds. Note that the reference pressure for defining the potential temperature is 1000 hPa, which is different from the surface pressure 1017.8 hPa. The large-scale divergence is set as $D = -3.75 \times 10^{-6} \text{ s}^{-1}$, and surface sensible heat and latent heat fluxes are set as 15 and 115 W m^{-2} , respectively. In absence of short-wave radiation during the night, the cooling/heating sources inside the cloud only come from long-wave radiation and are set as 65 W m^{-2} for cloud-top cooling and 17 W m^{-2} for cloud-base heating (Stevens *et al.*, 2005). The entrainment coefficients were set as typical values $B_0 = 2.5$, $B_1 = 0.2$, $B_3 = 0.44$, and $B_2k = 4$ as discussed in section 6. The effective mixing fraction is assumed to follow a beta distribution with mean and standard deviation linked by the

empirical function shown as thin solid line in Figure 4(b). The evolutions of the boundary-layer height and liquid water potential temperature with different distributions of mixing fraction are shown in Figure 6. Cloud-top mixing with low mixing fraction close to saturation mixing fraction has large evaporative cooling rate (Figure 2(b)) and thus tends to accelerate the growth of the boundary layer. These simulated boundary-layer heights are consistent with the observed cloud-top growth rate, showing 7.5 m h^{-1} growth rate as marked by the circles in Figure 6(a) (Stevens *et al.*, 2003). A faster boundary-layer growth rate allows more warm air from the free atmosphere to be entrained into the boundary layer thus increasing its temperature (Figure 6(b)).

8. Conclusions

We have introduced a simple cloud-top entrainment parametrization scheme to address the contribution of cloud-top evaporative cooling to the entrainment flux, one of the most important cloud drivers. We then quantified the evaporative cooling rate in a typical turbulent eddy and analyzed the cloud-top mixing process in terms of the effective mixing fraction defined as the fraction of air coming from the free atmosphere that enhances entrainment flux. Based on the results of Mellado *et al.* (2010b) and de Lozar and Mellado (2015a), we adopted the effective mixing fraction as a random variable, described by a beta distribution as suggested both by existing flight observations and recent numerical simulations.

The quantification of the evaporative cooling rate and a simple cloud-top mixing scheme allow us to interpret various forms of CTEI criteria and their dependence on the shape parameters of the beta distribution. Discriminating stable and unstable clouds in the CTEI diagram could assist the choice of the shape parameters, which can be further used to extend cloud parametrization schemes. When parametrized in general circulation models (Deardorff, 1972), these cloud-top mixing schemes have the potential to improve simulation of cloud dynamics and thus reduce the uncertainties in climate predictions.

Acknowledgements

This work was supported by the Duke Wireless Intelligent Sensor Networks (WiSeNet) Integrative Graduate Education and Research Training (IGERT) program through NSF Grant #DGE-1068871. We also acknowledge the financial support from National Science Foundation (NSF-EAR-0838301, NSF-EAR-1331846, and NSF-EAR-1316258). Comments by Juan-Pedro Mellado, Gabriel Katul, and three anonymous reviewers helped improve the paper. Data relating to this paper are available upon request.

Appendices

Appendix A: Cloud-topped boundary-layer model

Liquid water potential temperature and total water content are conserved quantities and thus may be assumed to be constant under both dry and moist adiabatic processes in the CTBL (Figure A1) (Lilly, 1968; Stage and Businger, 1981; Driedonks and Duynkerke, 1989; Pelly and Belcher, 2001). The liquid water potential temperature (θ_L) can be expressed with sufficient accuracy as (Betts, 1973; Garratt, 1992),

$$\theta_L = \theta - \frac{\lambda}{c_p} q_L, \quad (\text{A1})$$

where θ is potential temperature, λ is the latent heat of vaporization, and c_p is specific heat of air at constant pressure. The total water content (q_t) is defined as,

$$q_t = q_L + q, \quad (\text{A2})$$

where q is the specific humidity and q_L is the liquid water content. At the top of the boundary layer, sharp changes of temperature and humidity are observed and are readily approximated by jump discontinuities (Figure A1) (Lilly, 1968; Garratt, 1992).

The lifted condensation level (LCL) is assumed as the location of the cloud base, which separates the boundary layer into sub-cloud layer and cloud layer. Sounding profiles follow dry adiabatic process in the sub-cloud layer ($z < z_{\text{LCL}}$) and moist adiabatic process in the cloud layer ($z_{\text{LCL}} < z < h$).

Following Stull (1976), the governing equation for the mean variable of any property (ϕ) in a horizontally homogeneous turbulent flow (e.g. only vertical advection) can be expressed as

$$\frac{\partial \phi}{\partial t} + w_l \frac{\partial \phi}{\partial z} = \frac{1}{\rho c_p} \frac{\partial \bar{F}_\phi}{\partial z} - \frac{\partial \overline{w'\phi'}}{\partial z}, \quad (\text{A3})$$

where \bar{F}_ϕ is the horizontally averaged flux of ϕ and $\overline{w'\phi'}$ is the vertical turbulent flux of ϕ . For simplicity of conventional practice, the overbar for ϕ is not indicated. The mean large-scale vertical velocity w_l can be modelled as (Stull, 1988; Garratt, 1992; Ek and Mahrt, 1994)

$$w_l(z) = -Dz, \quad (\text{A4})$$

where D is the large-scale divergence, which is often assumed to be constant.

Replacing ϕ with θ_L and integrating (A3) with respect to z throughout the boundary layer using Leibnitz rule and integration by parts yields,

$$h \frac{d(\theta_L)}{dt} = (\overline{\theta_L'w'})_0 - (\overline{\theta_L'w'})_{h-} + \frac{\bar{R}}{\rho c_p}, \quad (\text{A5})$$

where

$$\langle \theta_L \rangle = \frac{1}{h} \int_0^h \theta_L(z) dz, \quad (\text{A6})$$

which is the mean liquid water potential temperature throughout the boundary layer. The subscripts h and 0 denote the flux location at the boundary-layer inversion and Earth surface, the net source term \bar{R} is the net radiation within the boundary layer (Appendix B), and the near-surface turbulent flux of liquid water potential temperature ($(\overline{\theta_L'w'})_0$) is simply near-surface sensible heat flux $(\overline{\theta'w'})_0$ since no liquid water exists near the earth surface $(q_L')_0 = 0$.

Similarly, replacing ϕ with q_t and integrating (A3) with respect to z throughout the boundary layer gives

$$h \frac{d\langle q_t \rangle}{dt} = (\overline{q_t'w'})_0 - (\overline{q_t'w'})_{h-}, \quad (\text{A7})$$

where

$$\langle q_t \rangle = \frac{1}{h} \int_0^h q_t(z) dz, \quad (\text{A8})$$

which is the mean total water content throughout the boundary layer. The near-surface turbulent flux of total water content $(\overline{q_t'w'})_0$ is simply near-surface latent heat flux $(\overline{q'w'})_0$ since $(q_L')_0 = 0$.

To find the entrainment flux $(\overline{\theta_L'w'})_{h-}$ and $(\overline{q_t'w'})_{h-}$ in (A5) and (A7), one can apply Leibnitz rule and integrate (A3) with respect to z between the boundary-layer top ($z = h-$) and the free atmosphere just above the boundary layer ($z = h+$). By replacing ϕ with conserved variable θ_L , the integration becomes

$$-(\overline{\theta_L'w'})_{h-} = \Delta \theta_L \left(\frac{dh}{dt} - w_l \right), \quad (\text{A9})$$

where $(dh/dt - w_l)$ is the average vertical velocity at height h . For the conserved variable q_t , the integration is,

$$-(\overline{q_t'w'})_{h-} = \Delta q_t \left(\frac{dh}{dt} - w_l \right). \quad (\text{A10})$$

The boundary layer growth rate (dh/dt) needs to be parametrized by other known variables to close the conservation (A5)–(A10) for the mixed-layer models as explained in section 2.

Appendix B: Radiation inside the clouds

Cloud-top long-wave radiative divergence, cloud-top short-wave radiative absorption, and cloud-base long-wave radiative heating as illustrated in Figure B1 are the three important radiation components inside the clouds which may have significant impacts on the boundary-layer states.

Near the cloud top, there is net long-wave radiative cooling which is the sum of upward and downward long-wave radiation,

$$\bar{R}_l^\uparrow - \varepsilon_l^\downarrow \bar{R}_l^\uparrow, \quad (\text{B1})$$

where \bar{R}_l^\uparrow is downward long-wave radiation from the free atmosphere above the cloud, ε_l^\downarrow is the downward long-wave absorptivity of the cloud, which is related to cloud properties such as liquid water path (Stephens, 1978b), and \bar{R}_l^\uparrow is the cloud-top upward long-wave radiation, which is determined by Stefan–Boltzmann law,

$$\bar{R}_l^\uparrow = \sigma \varepsilon_l^\uparrow \bar{T}_T^4, \quad (\text{B2})$$

where σ is the Stefan–Boltzmann constant, ε_l^\uparrow is the upward long-wave emissivity of the cloud (Stephens, 1978b), and \bar{T}_T is the temperature near the cloud top. Besides the net long-wave radiative cooling, clouds also partially absorb short-wave radiation, which depends on the incoming solar radiation and the short-wave absorptivity,

$$\varepsilon_s \bar{R}_s^\uparrow, \quad (\text{B3})$$

where \bar{R}_s^\uparrow is the part of the solar radiation that reaches free atmosphere above the cloud, and ε_s is the short-wave absorptivity of the cloud, which can be modelled as empirical functions of solar zenith angle and liquid water path (Stephens, 1978b). This heating may offset part of the long-wave radiative cooling (Rogers *et al.*, 1985) and thus the overall radiation at the cloud top can be expressed as

$$\bar{R}_c = \bar{R}_l^\uparrow - \varepsilon_l^\downarrow \bar{R}_l^\uparrow - \varepsilon_s \bar{R}_s^\uparrow. \quad (\text{B4})$$

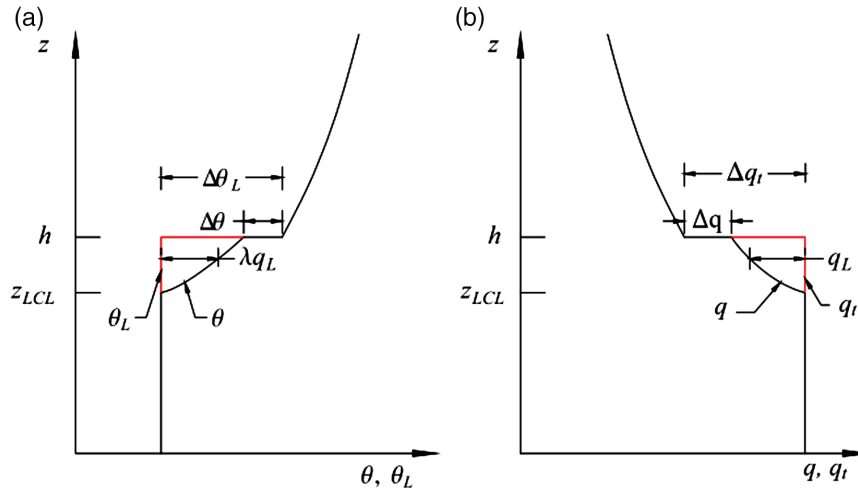


Figure A1. Schematic representation of the vertical profiles of (a) liquid water potential temperature and (b) total water content for the mixed CTBL model. [Colour figure can be viewed at wileyonlinelibrary.com].

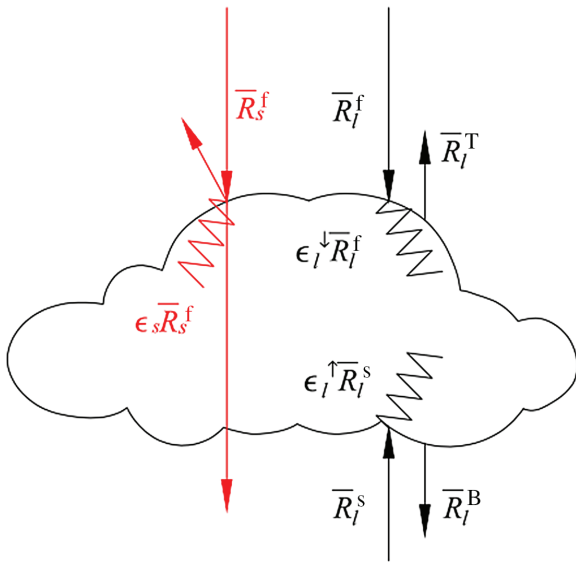


Figure B1. Components of radiation at the top and bottom of the cloud (red arrows are short-wave radiation; black arrows are long-wave radiation). [Colour figure can be viewed at wileyonlinelibrary.com].

This overall radiation loss takes place in a relatively thin layer near the cloud top (Rogers *et al.*, 1985; Garratt, 1992).

Near the cloud base, there is long-wave radiative heating under most circumstance,

$$\epsilon_i^{\uparrow} \bar{R}_l^s - \bar{R}_l^B, \quad (\text{B5})$$

where \bar{R}_l^s is long-wave radiation from sub-cloud layer, and \bar{R}_l^B is long-wave radiation leaving the cloud base, which is determined by the Stefan–Boltzmann law,

$$\bar{R}_l^B = \sigma \epsilon_i^{\downarrow} \bar{T}_B^4, \quad (\text{B6})$$

where \bar{T}_B is the temperature near the cloud base. The cloud-base radiative cooling is assumed to occur within a thin layer and is an order of magnitude smaller than the cloud-top radiative cooling \bar{R}_c . The overall radiation inside the cloud is the sum of all the heating and cooling sources,

$$\bar{R} = \epsilon_i^{\uparrow} \bar{R}_l^s - \bar{R}_l^B - \bar{R}_c. \quad (\text{B7})$$

This net radiation directly goes to the conservation (A5).

Appendix C: States of mixed air

For conserved variables of the mixed air, their quantities are linear functions of the effective mixing fraction during the cloud-top

moist adiabatic mixing (Betts and Albrecht, 1987)

$$\theta_{L,m} = (1 - \chi_e) \theta_{L,h-} + \chi_e \theta_{L,h+}, \quad (\text{C1})$$

and

$$q_{t,m} = (1 - \chi_e) q_{t,h-} + \chi_e q_{t,h+}. \quad (\text{C2})$$

To further find the non-conserved variables, the definitions in (A1) and (A2) are applied to the mixed air

$$\theta_m = \theta_{L,m} + \frac{\lambda}{c_p} q_{L,m}, \quad (\text{C3})$$

and

$$q_m = q_{t,m} - q_{L,m}, \quad (\text{C4})$$

where

$$q_{L,m} = \begin{cases} 0 & \text{if } q_m \leq q_m^* \\ q_{t,m} - q_m^* & \text{if } q_m > q_m^* \end{cases}, \quad (\text{C5})$$

where q_m^* is saturated specific humidity of the mixed air and is determined by Clausius–Clapeyron relation. After finding θ_m , q_m , $q_{L,m}$, one can calculate the virtual potential temperature of the mixed air as

$$\theta_{v,m} = \theta_m \left[1 + \left(\frac{R_v}{R_d} - 1 \right) q_m - q_{L,m} \right]. \quad (\text{C6})$$

For any given effective mixing fraction χ_e , (C1)–(C6) can be used to numerically calculate both the conserved and non-conserved variables of the mixed air.

Appendix D: Estimation of ζ

The ratio ζ in (21) depends on θ_m and $\theta_{v,m}$, which in turn depend nonlinearly on χ_e . These nonlinear relationships are described in (C1)–(C6) in Appendix C. Such behaviours are well approximated by piecewise linear functions (Kuo and Schubert, 1988; Duynkerke, 1993; Shao *et al.*, 1997; Lock and Macvean, 1999b; Yamaguchi and Randall, 2008)

$$\theta_{v,m}(\chi_e) = \begin{cases} \frac{\chi_e}{\chi^*} \theta_{v,m}(\chi^*) + \frac{\chi^* - \chi_e}{\chi^*} \theta_{v,h-} & \chi_e < \chi^* \\ \frac{1 - \chi_e}{1 - \chi^*} \theta_{v,m}(\chi^*) + \frac{\chi_e - \chi^*}{1 - \chi^*} \theta_{v,h+} & \chi_e \geq \chi^* \end{cases}, \quad (\text{D1})$$

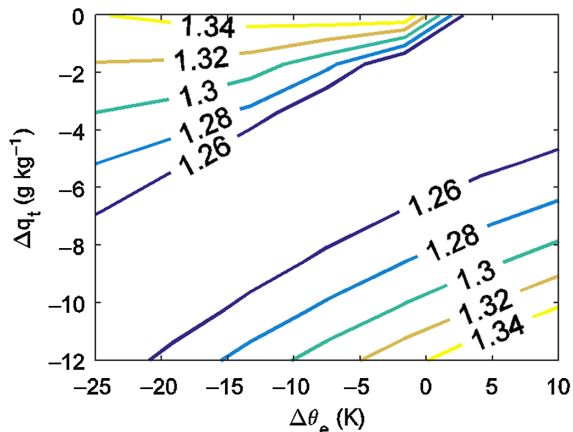


Figure D1. Contour plot of ζ in the $(\Delta\theta_e, \Delta q_t)$ plane. The boundary-layer variables are listed in the case K from Yamaguchi and Randall (2008). [Colour figure can be viewed at wileyonlinelibrary.com].

and

$$\theta_m(\chi_e) = \begin{cases} \frac{\chi_e}{\chi^*} \theta_m(\chi^*) + \frac{\chi^* - \chi_e}{\chi^*} \theta_{h-} & \chi_e < \chi^* \\ \frac{1 - \chi_e}{1 - \chi^*} \theta_m(\chi^*) + \frac{\chi_e - \chi^*}{1 - \chi^*} \theta_{h+} & \chi_e \geq \chi^* \end{cases} \quad (\text{D2})$$

where χ^* is the saturation mixing fraction, at which the mixed air is just saturated without any liquid water content. Substituting (D1) and (D2) into (21), one obtains

$$\zeta = \frac{(1 - \chi^*)\theta_{h-} + \chi^* \theta_{h+} - \theta_m(\chi^*)}{(1 - \chi^*)\theta_{v,h-} + \chi^* \theta_{v,h+} - \theta_{v,m}(\chi^*)}, \quad (\text{D3})$$

where the ratio ζ now becomes independent of χ_e . This ratio ζ has small variations around a typical value of 1.26 under various cloud conditions as shown in the $(\Delta\theta_e, \Delta q_t)$ plane in Figure D1.

Appendix E: Cloud-top entrainment instability

The sign and magnitude of the buoyancy reversal in the cloud-top mixing is represented by the virtual potential temperature difference between mixed air and the surrounding clouds $\theta_{v,m}(\chi_e) - \theta_{v,h-}$. While a positive difference tends to preserve a stable mixed layer, a negative difference may induce self-sustained downdraughts and lead to an unstable boundary layer. For this reason, $\theta_{v,m}(\chi_e) - \theta_{v,h-}$ is often used to define CTEI to evaluate the instability of the boundary layer in various studies by assuming different ways of mixing in terms of effective mixing fraction χ_e . For example, with the assumption that $\chi_e = \chi^*$ is the most important mixing fraction in the mixing process, Randall (1980) and Deardorff (1980b) defined the CTEI as

$$\Delta_{RD} = \frac{\theta_{v,m}(\chi^*) - \theta_{v,h-}}{\chi^*}, \quad (\text{E1})$$

and $\Delta_{RD} < 0$ indicates the CTBL is unstable. Assuming all values of χ_e are equally important, Nicholls and Turton (1986) defined Δ_{NT} as

$$\Delta_{NT} = 2 \int_0^1 [\theta_{v,m}(\chi_e) - \theta_{v,h-}] d\chi_e, \quad (\text{E2})$$

where the factor 2 makes sure that $\Delta_{NT} = \Delta\theta_v$ in the cloud-free case. Duynkerke (1993) argued that $(\theta_{v,m}(\chi_e) - \theta_{v,h-})/\chi_e$ rather than $\theta_{v,m}(\chi_e) - \theta_{v,h-}$ is a more important variable for evaluating cloud instability and defined the CTEI as

$$\Delta_D = \int_0^1 \frac{\theta_{v,m}(\chi_e) - \theta_{v,h-}}{\chi_e} d\chi_e, \quad (\text{E3})$$

and $\Delta_D < 0$ suggests the CTBL is unstable.

References

- Albrecht BA, Penc RS, Schubert WH. 1985. An observational study of cloud-topped mixed layers. *J. Atmos. Sci.* **42**: 800–822, doi: 10.1175/1520-0469(1985)042<0800:AOSOCT>2.0.CO;2.
- Albrecht BA, Randall DA, Nicholls S. 1988. Observations of marine stratocumulus clouds during FIRE. *Bull. Am. Meteorol. Soc.* **69**: 618–626, doi: 10.1175/1520-0477(1988)069<0618:OOMSCD>2.0.CO;2.
- Árnason G, Greenfield RS. 1972. Micro- and macro-structures of numerically simulated convective clouds. *J. Atmos. Sci.* **29**: 342–367, doi: 10.1175/1520-0469(1972)029<0342:MAMSON>2.0.CO;2.
- Betts AK. 1973. Non-precipitating cumulus convection and its parameterization. *Q. J. R. Meteorol. Soc.* **99**: 178–196, doi: 10.1002/qj.49709941915.
- Betts AK. 2009. Land-surface-atmosphere coupling in observations and models. *J. Adv. Model. Earth Syst.* **1**: 4, doi: 10.3894/james.2009.1.4.
- Betts AK, Albrecht BA. 1987. Conserved variable analysis of the convective boundary layer thermodynamic structure over the tropical oceans. *J. Atmos. Sci.* **44**: 83–99, doi: 10.1175/1520-0469(1987)044<0083:CVAOTC>2.0.CO;2.
- Bony S, Colman R, Kattsov VM, Allan RP, Bretherton CS, Dufresne J-L, Hall A, Hallegatte S, Holland MM, Ingram W, Randall DA, Soden DJ, Tselioudis G, Webb MJ. 2006. How well do we understand and evaluate climate change feedback processes? *J. Clim.* **19**: 3445–3482, doi: 10.1175/JCLI3819.1.
- Bony S, Dufresne J-L. 2005. Marine boundary layer clouds at the heart of tropical cloud feedback uncertainties in climate models. *Geophys. Res. Lett.* **32**: L20806, doi: 10.1029/2005GL023851.
- Boucher O, Randall D, Artaxo P, Bretherton C, Feingold G, Forster P, Kerminen V-M, Kondo Y, Liao H, Lohmann U, Rasch P, Satheesh SK, Sherwood S, Stevens B, Zhang XY. 2013. Clouds and aerosols. In *Climate Change 2013: The Physical Science Basis. Contribution of Working Group I to the Fifth Assessment Report of the Intergovernmental Panel on Climate Change*, Stocker TF, Qin D, Plattner G-K, Tignor M, Allen SK, Boschung J, Nauels A, Xia Y, Bex V, Midgley PM. (eds.): 571–658. Cambridge University Press: Cambridge, UK and New York, NY.
- Davison AC. 2003. *Statistical Models*. Cambridge University Press: Cambridge, UK.
- Deardorff JW. 1972. Parameterization of the planetary boundary layer for use in general circulation models I. *Mon. Weather Rev.* **100**: 93–106.
- Deardorff JW. 1976. On the entrainment rate of a stratocumulus-topped mixed layer. *Q. J. R. Meteorol. Soc.* **102**: 563–582, doi: 10.1002/qj.49710243306.
- Deardorff J. 1980a. Stratocumulus-capped mixed layers derived from a three-dimensional model. *Boundary-Layer Meteorol.* **18**: 495–527, doi: 10.1007/BF00119502.
- Deardorff JW. 1980b. Cloud-top entrainment instability. *J. Atmos. Sci.* **37**: 131–147, doi: 10.1175/1520-0469(1980)037<0131:CTEI>2.0.CO;2.
- Driedonks AGM, Duynkerke PG. 1989. Current problems in the stratocumulus-topped atmospheric boundary layer. *Boundary-Layer Meteorol.* **46**: 275–303, doi: 10.1007/BF00120843.
- Duynkerke PG. 1993. The stability of cloud top with regard to entrainment: Amendment of the theory of cloud-top entrainment instability. *J. Atmos. Sci.* **50**: 495–502, doi: 10.1175/1520-0469(1993)050<0495:TSOCTW>2.0.CO;2.
- Ek MB, Holtslag AAM. 2004. Influence of soil moisture on boundary-layer cloud development. *J. Hydrometeorol.* **5**: 86–99, doi: 10.1175/1525-7541(2004)005<0086:IOSMOB>2.0.CO;2.
- Ek M, Mahrt L. 1994. Daytime evolution of relative humidity at the boundary-layer top. *Mon. Weather Rev.* **122**: 2709–2721, doi: 10.1175/1520-0493(1994)122<2709:Deorha>2.0.CO;2.
- Emanuel KA. 1994. *Atmospheric convection*. Oxford University Press: New York, NY.
- Garratt JR. 1992. *The Atmospheric Boundary Layer*. Cambridge University Press: Cambridge, UK.
- Gentine P, Betts AK, Lintner BR, Findell KL, van Heerwaarden CC, D’Andrea F. 2013a. A probabilistic bulk model of coupled mixed layer and convection. Part II: Shallow convection case. *J. Atmos. Sci.* **70**: 1557–1576, doi: 10.1175/JAS-D-12-0146.1.
- Gentine P, Betts AK, Lintner BR, Findell KL, van Heerwaarden CC, Tzella A, D’Andrea F. 2013b. A probabilistic bulk model of coupled mixed layer and convection. Part I: Clear-sky case. *J. Atmos. Sci.* **70**: 1543–1556, doi: 10.1175/JAS-D-12-0145.1.
- Houze RA. 1993. *Cloud Dynamics*. Academic Press: Cambridge, MA.
- Juang J-Y, Katul GG, Porporato A, Stoy PC, Siqueira MS, Detto M, Kim H-S, Oren R. 2007. Eco-hydrological controls on summertime convective rainfall triggers. *Global Change Biol.* **13**: 887–896, doi: 10.1111/j.1365-2486.2006.01315.x.
- Kuo H-C, Schubert WH. 1988. Stability of cloud-topped boundary layers. *Q. J. R. Meteorol. Soc.* **114**: 887–916, doi: 10.1002/qj.49711448204.
- Lilly DK. 1968. Models of cloud-topped mixed layers under a strong inversion. *Q. J. R. Meteorol. Soc.* **94**: 292–309, doi: 10.1002/qj.49709440106.
- Lilly DK. 2002a. Entrainment into mixed layers. Part I: Sharp-edged and smoothed tops. *J. Atmos. Sci.* **59**: 3340–3352, doi: 10.1175/1520-0469(2002)059<3340:EIMLPI>2.0.CO;2.
- Lilly DK. 2002b. Entrainment into mixed layers. Part II: A new closure. *J. Atmos. Sci.* **59**: 3353–3361, doi: 10.1175/1520-0469(2002)059<3353:EIMLPI>2.0.CO;2.

- Lock AP. 1998. The parametrization of entrainment in cloudy boundary layers. *Q. J. R. Meteorol. Soc.* **124**: 2729–2753, doi: 10.1002/qj.49712455210.
- Lock AP, Macvean MK. 1999a. The parametrization of entrainment driven by surface heating and cloud-top cooling. *Q. J. R. Meteorol. Soc.* **125**: 271–299, doi: 10.1002/qj.49712555315.
- Lock AP, Macvean MK. 1999b. The generation of turbulence and entrainment by buoyancy reversal. *Q. J. R. Meteorol. Soc.* **125**: 1017–1038, doi: 10.1002/qj.49712555513.
- de Lozar A, Mellado JP. 2015a. Evaporative cooling amplification of the entrainment velocity in radiatively driven stratocumulus. *Geophys. Res. Lett.* **42**: 7223–7229, doi: 10.1002/2015GL065529.
- de Lozar A, Mellado JP. 2015b. Mixing driven by radiative and evaporative cooling at the stratocumulus top. *J. Atmos. Sci.* **72**: 4681–4700, doi: 10.1175/JAS-D-15-0087.1.
- MacVean MK, Mason PJ. 1990. Cloud-top entrainment instability through small-scale mixing and its parameterization in numerical models. *J. Atmos. Sci.* **47**: 1012–1030, doi: 10.1175/1520-0469(1990)047<1012:CTEITS>2.0.CO;2.
- Martin GM, Johnson DW, Spice A. 1994. The measurement and parameterization of effective radius of droplets in warm stratocumulus clouds. *J. Atmos. Sci.* **51**: 1823–1842, doi: 10.1175/1520-0469(1994)051<1823:TMAPOE>2.0.CO;2.
- Mellado JP. 2010. The evaporatively driven cloud-top mixing layer. *J. Fluid Mech.* **660**: 5–36, doi: 10.1017/s0022112010002831.
- Mellado J, Stevens B, Schmidt H, Peters N. 2010a. Two-fluid formulation of the cloud-top mixing layer for direct numerical simulation. *Theor. Comput. Fluid Dyn.* **24**: 511–536, doi: 10.1007/s00162-010-0182-x.
- Mellado JP, Stevens B, Schmidt H, Peters N. 2010b. Probability density functions in the cloud-top mixing layer. *New J. Phys.* **12**: 085010.
- Moeng C-H, Sullivan PP, Stevens B. 1999. Including radiative effects in an entrainment rate formula for buoyancy-driven PBLs. *J. Atmos. Sci.* **56**: 1031–1049, doi: 10.1175/1520-0469(1999)056<1031:IREIAE>2.0.CO;2.
- Nicholls S, Turton JD. 1986. An observational study of the structure of stratiform cloud sheets: Part II. Entrainment. *Q. J. R. Meteorol. Soc.* **112**: 461–480, doi: 10.1002/qj.49711247210.
- Pelly JL, Belcher SE. 2001. A mixed-layer model of the well-mixed stratocumulus-topped boundary layer. *Boundary-Layer Meteorol.* **100**: 171–187, doi: 10.1023/A:1019215221726.
- Porporato A. 2009. Atmospheric boundary-layer dynamics with constant bowen ratio. *Boundary-Layer Meteorol.* **132**: 227–240, doi: 10.1007/s10546-009-9400-8.
- Randall DA. 1980. Conditional instability of the first kind upside-down. *J. Atmos. Sci.* **37**: 125–130, doi: 10.1175/1520-0469(1980)037<0125:CIOTFK>2.0.CO;2.
- Randall DA. 1984. Buoyant production and consumption of turbulence kinetic energy in cloud-topped mixed layers. *J. Atmos. Sci.* **41**: 402–413, doi: 10.1175/1520-0469(1984)041<0402:BPACOT>2.0.CO;2.
- Rigby JR, Yin J, Albertson J, Porporato A. 2015. Approximate analytical solution to diurnal atmospheric boundary-layer growth under well-watered conditions. *Boundary-Layer Meteorol.* **156**: 73–89, doi: 10.1007/s10546-015-0018-8.
- Rogers DP, Businger JA, Charnock H. 1985. A numerical investigation of the JASIN atmospheric boundary layer. *Boundary-Layer Meteorol.* **32**: 373–399, doi: 10.1007/BF00122001.
- Shao Q, Randall DA, Moeng C-H, Dickinson RE. 1997. A method to determine the amounts of cloud-top radiative and evaporative cooling in a stratocumulus-topped boundary layer. *Q. J. R. Meteorol. Soc.* **123**: 2187–2213, doi: 10.1002/qj.49712354403.
- Stage SA, Businger JA. 1981. A model for entrainment into a cloud-topped marine boundary layer. Part I: Model description and application to a cold-air outbreak episode. *J. Atmos. Sci.* **38**: 2213–2229, doi: 10.1175/1520-0469(1981)038<2213:AMFEIA>2.0.CO;2.
- Stevens GL. 1978a. Radiation profiles in extended water clouds. I: Theory. *J. Atmos. Sci.* **35**: 2111–2122, doi: 10.1175/1520-0469(1978)035<2111:RPIEWC>2.0.CO;2.
- Stevens GL. 1978b. Radiation profiles in extended water clouds. II: Parameterization schemes. *J. Atmos. Sci.* **35**: 2123–2132, doi: 10.1175/1520-0469(1978)035<2123:RPIEWC>2.0.CO;2.
- Stevens GL. 2005. Cloud feedbacks in the climate system: A critical review. *J. Clim.* **18**: 237–273, doi: 10.1175/JCLI-3243.1.
- Stevens B. 2002. Entrainment in stratocumulus-topped mixed layers. *Q. J. R. Meteorol. Soc.* **128**: 2663–2690, doi: 10.1256/qj.01.202.
- Stevens B. 2005. Atmospheric moist convection. *Annu. Rev. Earth Planet. Sci.* **33**: 605–643.
- Stevens B. 2006. Bulk boundary-layer concepts for simplified models of tropical dynamics. *Theor. Comput. Fluid Dyn.* **20**: 279–304.
- Stevens B, Lenschow DH, Faloona I, Moeng C-H, Lilly DK, Blomquist B, Vali G, Bandy A, Campos T, Gerber H, Haimov S, Morley B, Thornton C. 2003. On entrainment rates in nocturnal marine stratocumulus. *Q. J. R. Meteorol. Soc.* **129**: 3469–3493, doi: 10.1256/qj.02.202.
- Stevens B, Moeng C-H, Ackerman AS, Bretherton CS, Chlond A, de Roode S, Edwards J, Golaz J-C, Jiang H, Khairoutdinov M, Kirkpatrick MP, Lewellen DC, Lock A, Müller F, Stevens DE, Whelan E, Zhu P. 2005. Evaluation of large-eddy simulations via observations of nocturnal marine stratocumulus. *Mon. Weather Rev.* **133**: 1443–1462, doi: 10.1175/MWR2930.1.
- Stull RB. 1976. The energetics of entrainment across a density interface. *J. Atmos. Sci.* **33**: 1260–1267, doi: 10.1175/1520-0469(1976)033<1260:TEOEAD>2.0.CO;2.
- Stull RB. 1988. *An Introduction to Boundary-Layer Meteorology*. Kluwer Academic Publishers: Dordrecht, The Netherlands.
- Sullivan PP, Moeng C-H, Stevens B, Lenschow DH, Mayor SD. 1998. Structure of the entrainment zone capping the convective atmospheric boundary layer. *J. Atmos. Sci.* **55**: 3042–3064, doi: 10.1175/1520-0469(1998)055<3042:SOTEZC>2.0.CO;2.
- Tennekes H. 1973. A model for the dynamics of the inversion above a convective boundary layer. *J. Atmos. Sci.* **30**: 558–567, doi: 10.1175/1520-0469(1973)030<0558:AMFTDO>2.0.CO;2.
- Turton JD, Nicholls S. 1987. A study of the diurnal variation of stratocumulus using a multiple mixed-layer model. *Q. J. R. Meteorol. Soc.* **113**: 969–1009, doi: 10.1002/qj.49711347712.
- Wang Q, Albrecht BA. 1994. Observations of cloud-top entrainment in marine stratocumulus clouds. *J. Atmos. Sci.* **51**: 1530–1547, doi: 10.1175/1520-0469(1994)051<1530:OOCTEI>2.0.CO;2.
- Wood R. 2012. Stratocumulus clouds. *Mon. Weather Rev.* **140**: 2373–2423, doi: 10.1175/MWR-D-11-00121.1.
- Yamaguchi T, Feingold G. 2013. On the size distribution of cloud holes in stratocumulus and their relationship to cloud-top entrainment. *Geophys. Res. Lett.* **40**: 2450–2454, doi: 10.1002/grl.50442.
- Yamaguchi T, Randall DA. 2008. Large-Eddy simulation of evaporatively driven entrainment in cloud-topped mixed layers. *J. Atmos. Sci.* **65**: 1481–1504, doi: 10.1175/2007JAS2438.1.
- Yamamoto G, Tanaka M, Asano S. 1970. Radiative transfer in water clouds in the infrared region. *J. Atmos. Sci.* **27**: 282–292, doi: 10.1175/1520-0469(1970)027<0282:RTIWCI>2.0.CO;2.
- Yin J, Albertson JD, Rigby JR, Porporato A. 2015. Land and atmospheric controls on initiation and intensity of moist convection: CAPE dynamics and LCL crossings. *Water Resour. Res.* **51**: 8476–8493, doi: 10.1002/2015wr017286.
- Yue Q, Kahn BH, Xiao H, Schreier MM, Fetzer EJ, Teixeira J, Sušelj K. 2013. Transitions of cloud-topped marine boundary layers characterized by AIRS, MODIS, and a large-eddy simulation model. *J. Geophys. Res. Atmos.* **118**: 8598–8611, doi: 10.1002/jgrd.50676.
- Zhang M, Bretherton CS, Blossey PN, Austin PH, Bacmeister JT, Bony S, Briant F, Cheedela SK, Cheng A, Del Genio AD, De Roode SR, Endo S, Franklin CN, Golaz J-C, Hannay C, Heus T, Isotta FA, Dufresne J-L, Kang I-S, Awai H, Köhler M, Larson VE, Liu Y, Lock AP, Lohmann U, Khairoutdinov MF, Molod AM, Neggers RAJ, Rasch P, Sandu I, Senkbeil R, Siebesma AP, Siegenthaler-Le Drian C, Stevens B, Suarez MJ, Xu K-M, von Salzen K, Webb MJ, Wolf A, Zhao M. 2013. CGILS: Results from the first phase of an international project to understand the physical mechanisms of low cloud feedbacks in single-column models. *J. Adv. Model. Earth Syst.* **5**: 826–842, doi: 10.1002/2013MS000246.